Impact of Carbon Support Meso-Porosity on Mass Transport and Performance of PEMFC Cathode Catalyst Layers

Sebastian Ott,[a] Andreas Bauer,[b] Fengmin Du,[b] Tuan Anh Dao,[b] Malte Klingenhof,[a] Alin Orfanidi,*[b] and Peter Strasser*[a]

The analysis of the impact of the cathode catalyst layer pore structure on the membrane electrode assembly (MEA) cell performance of a PEMFC is presented. In this study, a pristine CMK-3 catalyst carbon support material with well-defined pore structure in the 3–6 nm range together with two nitrogen-doped variants is analyzed against a commercial carbon black to achieve a better understanding of catalyst layer porosity-performance relations. We used chemically N-doped CMK-3 catalyst to learn more about the effect of N-doped porous catalyst supports on the concomitant transport properties and PEMFC cell performance. Chemical treatment using cyanamide was conducted to introduce a variety of N-functionalities. A detailed in-situ electrochemical investigation was combined with N_2-physisorption analysis. Based on their structural properties, the mesopore fractions and pore openings display a major role for reducing oxygen transport resistance and enhance Pt accessibility. We find that hierarchically ordered mesoporosity is superior to disordered porosity with prevalent micropore character: Analysis including adsorption electrochemical active surface area (ECSA), Pt-accessibility, ionomer coverage, pore geometry, proton resistivity and transport loss we conclude the importance of a well-defined mesoporous structure for its cell performance.

Introduction

In the global fight against climate change, the reduction of greenhouse gas emission is a major strategy. One fraction of the human made emissions lies in the transport section for short and long-range transportation. To reduce the CO_2 emission of the transport sector, fuel cell technology provides a big potential as power source for zero net emission in future economy and infrastructure. Even though fuel cell electrical vehicle (FCEVs) gathered increased attention due to their short refueling time and long distance range, their wider commercial spread is still hindered compared to battery electrical vehicles (BEVs) and internal combustion engine vehicles (ICEVs). One major issue lies in the cost intensive production line of the components especially in the need of noble metals such as Pt. The high demand of catalytic active sites breaks down to the sluggish ORR on the cathode side of a fuel cell and transport limitations throughout the catalytic layer itself. According to the DOE targets, the Pt loading needs to be reduced below 0.1 $mg_{Pt}cm^{-2}$ to enable an economic and ecologic efficient mass scale-up production line of FCEVs.[1] To achieve this target, many researchers' efforts were made to increase the catalytic activity of the metal specie by dealloying, shape controlling etc.[2] However, the significant role of the supporting material and their tuning potential towards performance enhancement has only recently started to gain attention.

High surface area carbon ($>800\ m^2g^{-1}$) is used to enable an increased mass activity by minimizing poisoning of the active sites originating from the sulfonic acid groups of the ionomer, since direct metal/ionomer contact can be reduced compared to low surface area carbons.[3] However, utilizing a well-developed porous support material, where the active metal sites are mainly located in the interior of the carbon support, causes mass transport limitations.[4] As a result of this, the catalytic material suffers from oxygen depletion and concomitant oxygen mass transport losses at high current densities. A number of studies have been put forward in recent years to analyze and mitigate the detrimental catalyst layer transport effects. Therein, a number of different aspects were identified to contribute to the observed performance losses, especially for low Pt loading based electrodes. The influence of the electrochemical active surface area (ECSA) was found to directly determine the magnitude of the local oxygen flux.[5] In addition, the catalyst support-ionomer interaction was shown to affect the spatial distribution of the ionomer, which in turn strongly affect the proton and oxygen transport characteristics of the catalyst layers.[6] Kodama et al. provided the first structural

[a] S. Ott, M. Klingenhof, Prof. P. Strasser
Department of Chemistry
Chemical Engineering Division
Technical University of Berlin
Straße des 17 Juni 124
10623 Berlin (Germany)
E-mail: pstrasser@tu-berlin.de
[b] A. Bauer, F. Du, T. A. Dao, A. Orfanidi
BMW Group
80788 Munich (Germany)
E-mail: alin.orfanidi@bmw.de

Supporting information for this article is available on the WWW under https://doi.org/10.1002/cctc.202101162

© 2021 The Authors. ChemCatChem published by Wiley-VCH GmbH. This is an open access article under the terms of the Creative Commons Attribution License, which permits use, distribution and reproduction in any medium, provided the original work is properly cited.

evidence associating the presence of dense ionomer layers over the catalytic active metal sites with a so-called local oxygen transport resistance.[7] The importance of the homogenous ionomer distribution towards improvement of transport phenomena and increase in cell performance was also recently demonstrated in the previous publication by Ott et al.[6b] At the same time, the porosity of both the support material and the resulting catalytic layer plays an important role, building up the pathway oxygen molecules have to travel trough.

To gain deeper insights into the role of the catalyst support within the catalytic layer and the influence of their porosity towards mass activity and oxygen mass transport resistance, Yarlagadda et al. investigated fine-tuned carbon support materials.[8] They were able to show that utilizing a carbon material with accessible pores in a range of 4–7 nm improved both mass transport and catalyst activity. Based on their findings, metal active sites within pores of such "accessible" dimensions would provide an optimized trade-off between reduced poisoning effect (from the ionomer in direct contact with the active sites) and improved oxygen transport through the catalytic layer reaching the metal surface. By contrast, Ramaswamy et al. focused on the correlation of micropores (<2 nm) and macropores (here defined as >8 nm) with the cell performance.[9] They hypothesized a correlation of the micropore surface area with the extension of bottleneck openings throughout the carbon structure. Whereas a decreased ratio of macropores would reduce the carbon support surface area available for ionomer interaction, this may favor a more homogeneous ionomer distribution. Consequently, both parameters, namely micro- and meso/macroporous fraction, would influence oxygen mass transport phenomena and thus directly determine the fuel cell performance at high current densities. These two studies by Yarlagadda et al. and Ramaswamy et al. provide us valuable guidelines on how to tune the mesopores of the catalyst support, with the aim to achieve increased mass activity and improve performance by reducing the micropore surface area in non-hierarchically ordered porous structured carbon.

To close the knowledge gap between those two studies, in the present contribution, we investigated the influence of pristine and N-doped carbon supports with well-defined mesoporous structure on the overall PEMFC cell performance. By using an ordered/templated mesoporous carbon with well-defined pore structure, in particular CMK-3, we were able to correlate performance changes with pore properties of the carbon support. A commercial high surface area carbon (Ketjenblack) was also used in the present study for comparison reasons, as it is a widely used as carbon support in fuel cells applications. A thermal process using a solid N precursor enabled concomitant pore tuning and N-modification of the CMK-3 carbons. We conducted electrochemical characterization of nanoparticle Pt catalysts supported on our tailored N-doped mesoporous supports and referenced them to the pristine carbon material. The identification of oxygen mass transport resistance, ECSA and performance under different relative humidity (RH) conditions provides information about transport phenomena within the catalytic layer. In combination with structural modified carbon material, we are able to deconvolute the influence of specific porous characteristics towards the membrane electrode assembly (MEA) performance.

Experimental

Synthesis

For the carbon pre-oxidation step, a batch of 500 mg commercial CMK-3 (ACS material) was mixed in a 50 mL flask with 25 mL 70% HNO_3 (VWR chemicals, AnalaR NORMAPUR). The mixture was continuously stirred under reflux for 30 min and immersed in a 70 °C pre heated oil bath. The resulting powder was filtrated and washed with water until pH neutrality and dried in a vacuum oven at 80 °C for 17 h. The pre-oxidized carbon was denoted as CMK-3Ox.

For the N-functionalization, 200 mg CMK-3 and CMK-3Ox were mixed with 17 mg and 12 mg Cyanamid, respectively. The mixture was diluted in 4 mL water and sonicated for 15 min to ensure a homogenous precursor distribution. The suspension was then frozen in liquid nitrogen and the water content evaporated in a freeze dryer overnight. For final heat treatment, the resulting powder was set in a tube furnace (CARBOLITE GERO GmbH & Co KG, Germany) and treated up to 600 °C. After an initial purging step of 15 min with Ar, a heating ramp of 400 K/h was set until the temperature reached 600 °C and was held for 2 h before naturally cooled down to room temperature. A constant gas flow rate of 10 L/h was kept for the Ar flow. The obtained powders were denoted as CMK-3/CA and CMK-3Ox/CA.

A commercial Ketjenblack EC-300j (here denoted as KB) was purchased from AkzoNobel and used in the present study for comparison reasons. For Pt-deposition 150 mg of the N-modified (CMK-3/CA and CMK-3Ox/CA) or pristine carbon (CMK-3 and KB) support was mixed with 100 mL ethylene glycol (99.8%, Sigma-Aldrich) and 50 mL deionized water in a 250 mL round bottom flask.[6a] The mixture was bath-sonicated for 15 min before adding H_2PtCl_6 solution (0.25 mol/L, obtained from solid $H_2PtCl_6 \cdot 6H_2O$, Alfa Aesar) solution, whose amount was adjusted to match a nominal loading of 14–20 wt.%. The mixture was continuously stirred under reflux for 2 h and immersed in a 120 °C pre heated oil bath. The resulting powder was filtrated and washed with water until all Cl-residues were removed (3 L water per 200 mg catalyst) and thereafter dried in a vacuum over at 80 °C for 17 h. The exact Pt loading for each catalyst was determined using inductively coupled plasma-optical emission spectrometry ICP-OES and shown in Table 2.

Physico-chemical characterization

Elemental analysis was applied to determine the exact carbon supports composition. Therefore, a Thermo Flash 1112 Organic Elemental Analyzer (Thermo Finnigan) was used. The samples were combusted in presence of V_2O_5 (as oxidizer) by dynamic flash at 1020 °C. The decomposition takes place in a manually stacked reactor of $WO_3/Cu/Al_2O_3$ layers. Gas chromatography (GC) determines and quantifies the resulting gases. The elemental analysis of C, H, N, and S of different carbon supports is given in Table 1.

The exact Pt content was determined via inductively coupled plasma (ICP) analysis using a VARIAN 715-ES system. Around 7 mg of the final catalyst was placed in a microwave tube and mixed with 2 mL H_2SO_4 (95–98%, VWR chemicals, AnalaR NORMAPUR), 2 mL HNO_3 (69%, VWR chemicals, AnalaR NORMAPUR) and 6 mL

© 2021 The Authors. ChemCatChem published by Wiley-VCH GmbH

Table 1. Elemental bulk composition (CHN) of the different types of carbons. The oxygen content was estimated as the difference to 100% assuming only C, N, H and O atoms in the carbon species.

Sample	Elemental analysis [wt%] C	N	H	O
KB	98.57	0	0	1.43
CMK-3Ox	85.07	0.50	0.16	14.27
CMK-3/CA	86.51	0.78	0.24	12.47
CMK-3Ox/CA	94.09	1.29	0.12	4.50

HCl (37%, VWR chemicals, AnalaR NORMAPUR). All Pt particles were dissolved during the microwave (Microwave GO, ANTON PAAR) heat treatment, where the running protocol comprised of applying a heating ramp up to 120 °C within 10 min and hold for another 10 min before cooling down to room temperature. From the standard solutions of 1 mg/L, 5 mg/L and 10 mg/L (H_2PtCl_6 in 2 mol/L HCl, 1000 mg/L Pt, MERCK KGAA), a calibration curve was constructed and the chosen wavelengths for the Pt determination were 203.646 nm, 204.939 nm, 212.863 nm, 214.424 nm, 217.468 nm and 224.552 nm. The results are depicted in Table 2.

N_2 physisorption was conducted to investigate the micro and meso pore structure of the carbon species using Autosorb-1 (Quantachrome Instruments). A 4 mm diameter glass tube was stacked with the sample, glass wool and a glass rod to minimize the dead volume. The sample weight was adjusted so that the absolute surface area exceeds 10 m^2 in order to minimize the errors of the measurement. To remove all gas and water residues adsorbed at the carbon surface the sample was degassed under vacuum at 80 °C for at least 24 h. The adsorption and desorption isotherms were recorded in a range of $10^{-5} \leq p/p_0 \leq 0.995$ with p_0 referring to the saturation pressure and p the actual gas pressure. To be able to distinguish between micropores (< 2 nm) to mesopores (> 2 nm) and avoid any artificial gaps the choice of a matching Density Functional Theory (DFT) kernel combined with a fitting model is important. In case of Ketjenblack (KB), a Quenched Solid Density Functional Theory (QSDFT) kernel with a slit/cylindrical pores model was applied for the adsorption branch. In case of CMK-3 based supports a non-local density functional theory (NLDFT) kernel with a cylindrical pore of the equilibrium model was applied. The latter model was considered more suitable as template carbon species of CMK-3 provides more defined and structured carbon particles as opposed to the amorphous Ketjenblack carbon.[10]

The effective ionomer film thickness is calculated based on the equation 5a and 5c of Liu et al.[11] For this calculation and the investigation of ionomer distribution in the catalyst layers the catalyst powder (Pt + carbon support) and the catalyst powder coated with ionomer were also analyzed using N_2 physisorption while QSDFT kernels with cylindrical pore model was used for the adsorption branch. The catalyst void volume below 4 nm correlates with the volume of intruded ionomer and can be considered as not taking part in the exterior film thickness. The exterior pore surface is defined as carbon support surface above 4 nm.

Table 2. Cathode specifications of 5 cm^2 MEAs: Pt catalyst loading on different carbon supports and the cathode Pt loading.

Catalyst type	Pt catalyst loading [wt.%]	Cathode Pt loading [mg_{Pt}/cm^2]
Pt/KB	16.1 ± 0.5	0.115 ± 0.008
Pt/CMK-3	20.6	0.140 ± 0.002
Pt/CMK-3/CA	19.3	0.120
Pt/CMK-3Ox/CA	14.2	0.135 ± 0.005

To determine the Pt crystallite size, X-ray powder diffraction (XRD) measurement was conducted. A BRUKER D8 ADVANCE diffractometer with a single beam and a Cu-$K_{\alpha 1}$ ($\gamma = 1.54051$ Å) source was used. The samples were grinded and placed on a Si waver before scanning from 20–90° without rotation using a scan rate of 0.04° per 7 s.

Transmission electron microscope (TEM) measurements were conducted using a Tecnai G2 20 s-Twin microscope, equipped with a LaB_6-cathode and a GATAN MS794 P CCD-detector at ZELMI Centrum, Technical University of Berlin. TEM samples were ultrasonicated in *i*-PrOH and drop-dried on copper grids.

Membrane electrode assembly (MEA) testing

The decal transfer method was employed to manufacture all MEAs.[12] For the catalyst inks, a low-EW ionomer dispersed in 40% H_2O/60% 1-propanol (3 M™ Dyneon™ PFSA (725 EW≡ $g_{polymer}/mol_{H+}$)) was mixed with the catalyst powder. A specific water/1-propanol ratio of 16–25 wt.% H_2O in 1-propanol was applied for Ketjenblack based samples and 12–15 wt.% H_2O in 1-propanol for CMK-3 based ones. The ionomer to carbon ratio (I/C) was in all cases 0.65. After optimizing the ink recipe and viscosity to achieve high decal quality, all materials were merged in a 15 ml HDPE capped bottle containing 26 g of 5 mm ZrO_2 beads in the following sequence: catalyst, water, 1-propanol, and finally the ionomer dispersion. After roll-mixing for 18 h at a speed of 60 rpm at room temperature, the homogenously mixed ink was coated onto a virgin PTFE using a Mayer rod coater (ERICHSEN UNICOATER MODEL 490). The resulting cathode electrode loadings for each catalytic layer is given in Table 2.

To prevent any influence in voltage loss originating from the anodic electrode, a commercially available 30 wt.% Pt/graphitized-Ketjenblack (TEC10EA30E, TANAKA Kikinzoku Kogyo K. K.) was used to manufacture an anode with a I/C ratio of 0.65 and a Pt loading of 0.17 $mgPt/cm^2$. To determine the exact electrode loading the decal was weight before and after decal transfer. The decal transfer was done by hot pressing a 10 μm membrane (GORE MX20.10) between the anode and cathode decals at 155 °C for 3 min with 0.24 kN/cm^2 (hereby denoted as CCM). The anode and cathode decals had an active area of 8.25 cm^2. To accurately define the active area the MEA to 5 cm^2, the CCMs were additionally sandwiched between two subgaskets with an active area window of 5 cm^2 (CMC Klebetechnik, type: PEM-Schutzfolie 61325). The lamination process comprises of a first hot pressing step at 135 °C for 10 min under 0.135 kN/cm^2, followed by ramping down to 75 °C within 10 min without releasing the applied force.

A modified single-cell hardware from Tandem Technologies containing a 50 cm^2 active area graphite composite flow field (14 channel serpentine flow field[13] purchased from Nisshinbo) was used for all electrochemical testing (the flow field and adjustment of the MEA is shown in Figure S4). A hardstop sealing approach is used to define the compression of the MEA based on the thickness of the sealing layers (shown in Figure S3). The incompressible fiberglass-reinforced PTFE-gaskets (Fiberflon) was adjusted to obtain a 20% compression of the GDL (29BC with a nominal thickness of 235–240 μm; SGL Carbon) by applying 9 bar clamping pressure on the cell. All fuel cell measurements were conducted on an automated HORIBA FuelCon GmbH (Germany) single cell test station (typ 200 A FUELCON) equipped with a potentiostat (ZAHNER-Elektrik GmbH & CoKG) coupled with a booster. Pure hydrogen (99.999% purity) and compressed air were used as anode and cathode reactant, respectively. For each type of MEA, two independent fuel cell measurements were performed and the

© 2021 The Authors. ChemCatChem published by Wiley-VCH GmbH

average value with corresponding error bars as the standard deviation is depicted in all figures.

All MEAs were activated, using a conditioning protocol from DOE, were the voltage was cycled 8x times between OCV (5 min), 0.85 V (10 min) and 0.6 V (45 min) at 80 °C cell temperature, 90 % RH and 170 kPa_{abs} under differential flows.[6b] The MEA performance was determined via polarization curves conducted under differential flows (H_2/air = 1.0/2.0 Nl/min) at both dry (90 °C cell temperature, 30 % RH and 170 kPa_{abs}) and wet (60 °C cell temperature, 90 % RH and 170 kPa_{abs}) operating conditions.[14] The ECSA was evaluated via CO stripping at a cell temperature of 80 °C at different relative humidities (30 % and 100 % RH).[6b] In addition, proton conductivity of the cathodic catalyst layer was evaluated via EIS with peak-to-peak perturbation of 20 mV, where the cell was kept under H_2 flow (1.0 Nl/min) at the anode and N_2 flow (2.0 Nl/min) at the cathode, cell temperature of 80 °C, and cathode voltage at 0.5 V.[14] The determination of the specific proton resistivity (ρ, in Ω cm) via fitting of the transmission line model was the same as described in detail in Du et al.[14] The mass transport resistance was estimated via limiting current measurement using 2.4 % O_2/N_2 (2.045 Nl/min) at the cathode side and pure H_2 (1.0 Nl/min) at the anode side, where the testing conditions were: cell temperature was kept at 80 °C with two relative humidities (30 % RH and 100 % RH).[6b] All testing was done under differential flows. For extensive details on the testing protocols, please refer to our previously published papers cited next to each characterization method, as the exact same testing conditions were used in the present study.

Results and Discussion

The overarching goal of this work is the description and improved understanding of the impact of the mesopore structure of cathode catalyst carbonaceous support materials on the overall PEMFC cell performance. To achieve this goal, we used commercial Ketjenblack (EC 300j) as a reference carbon support and compared it to highly ordered template-based CMK-3 carbon materials with tuned, yet tailored mesoporosity. The well- defined mesoporous structure of pristine CMK-3 was tuned by applying a variety of synthetic N-modifications. The N modification synthesis step employed solid cyanamide as an N-precursor during an annealing treatment at 600 °C under Ar atmosphere (more details can be found in Experimental section above). This N-modified CMK-3 material will be referred to as "CMK-3/CA". From "CMK-3/CA", an oxidized variant of a N-modified CMK-3 support material was prepared by means of treatment with aqueous HNO_3, henceforth denoted as "CMK-3Ox/CA". The thermal protocol and other synthetic parameters of the N modified samples were modified to control the resulting weight-based nitrogen content, N wt % (Table 1), to comparable values in all materials. The Pt-based catalysts supported on such modified carbons reveal an overall homogenous and similar Pt-particle distribution over the entire carbons' surface as proven by TEM (Figure S1). Additional XRD evaluation determine a Pt-crystallite size from 2.0–3.7 nm revealing the bigger Pt-particles on CMK-3Ox/CA (Figure S2 and Table S1.

Cathode catalyst support porosity

N_2 adsorption isotherms served to investigate the micro and mesoscale pore structure of the four differently prepared carbon supports. Table 1 shows the surface area values derived from a QSDFT (KB) and NLDFT (CMK-3 based carbons) analysis. Figure 1 depicts the differential surface area vs pore diameter of the four different carbon supports. The absolute surface area of the pristine carbon materials (CMK-3 and KB) are within a similar range, however, alter after the chemical N-modification. In the mesoporous region from 2–8 nm, the well-ordered pristine CMK-3 exposes all of its porosity (Table 3 and inset Figure 1), whereas Ketjenblack (KB) showed significant contributions of microporosity < 2 nm. The NLDFT surface area of CMK-3 somewhat declined after N-modification (Table 3). The latter might appear counter-intuitive, given the notion that the cyanamide annealing is expected to etch and oxidize surface carbon bonds by forming hydrocyanide vapor, creating additional microporosity.[15] In fact, this etching effect was evident by the significant increase in the microporous pore size range (< 2 nm) in Figure 1. However, the overall pore structure was nonetheless collapsing during the N-modification process, evidenced by the decline in the integral surface contribution in the mesopore region. The further decreased surface area of CMK-3Ox/CA compared to CMK-3/CA appeared to be caused by the reduced pore size fraction in the range above 8 nm.

The inset of Figure 1 shows the cumulative surface area indicating a shift of the step from micro to mesopores around 2.5 nm with the N-modification and type of carbon. It is evident from the Figure 1 inset that the unmodified CMK-3 revealed almost the entire pore structure in a range of 3–6 nm without any contribution from micropores. The other three samples revealed a comparable fraction of surface area within this range

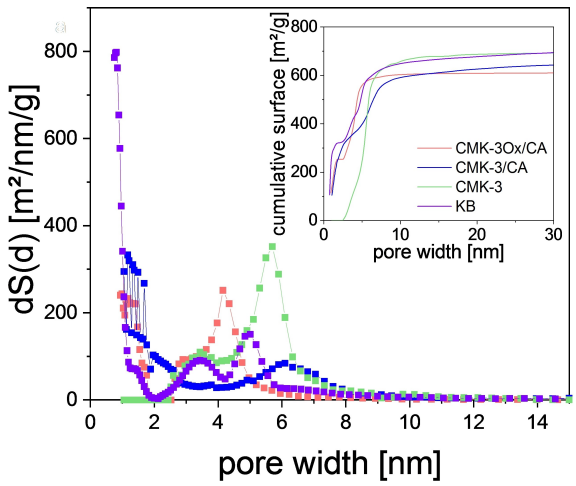

Figure 1. Pore area distributions of the carbon support material with different types of carbons (unmodified and N-functionalized) calculated by the DFT model (QSDFT for KB and NLDFT for CMK-3 based carbons) and based on the adsorption branch. The graph shows the derivative of the pore surface with respect to the pore diameter vs. the pore diameter for the different carbons. The inset shows the cumulative surface area with respect to the pore width in a range up to 30 nm. The absolute cumulative surface area calculated with this QSDFT-model is given in Table 3.

© 2021 The Authors. ChemCatChem published by Wiley-VCH GmbH

Table 3. Pore analysis of the DFT surface area (QSDFT for KB and NLDFT for CMK-3 based carbons), mesoporous surface area in the range 2–8 nm (S_{meso}), and pore opening on the primary particle.

Sample	$DFT_{surface\ area}$ [m^2/g]	Surface $area_{2-8nm}$ [m^2/g]	Pore opening [nm]	CL sample	Gravimetric stacking volume[a] [μm/(mg_C/cm^2)]	t_i^{eff} [b]
KB	736	301	4.98	Pt/KB	24 ± 2	0.22
CMK-3	696	630	5.67	Pt/CMK-3	27 ± 1	0.45
CMK-3/CA	653	307	6.08	Pt/CMK-3/CA	26 ± 1	0.75
CMK-3Ox/CA	613	346	4.17	Pt/CMK-3Ox/CA	28 ± 1	1.27

[a] Gravimetric stacking volume of the catalyst layers calculated from cross section determination for each type of MEA used in the present study. [b] Effective ionomer film thickness (t_i^{eff}) corrected for the ionomer intruded into the interior voids (pores < 4 nm) of the primary particle determined by N-physisorption.

from 300 to 350 m^2/g. However, a closer look at the pore size distribution clearly shows their striking difference in mesopore structure. CMK-3 is a cylindrical constructed carbon thus making the pores accessible via an opening in a similar size to the cylindrical shaped pore. This pore opening is determined as the maximum peak in the pore size distribution plot (Figure 1). This maximum peak of the pore width is clearly shifted by the N-modification process. Therefore, it seems that pre-treatment with acid shrinks the pore openings what can be explained by creation of some carboxylic groups at the graphene sheet edges. Consequently, those surface attached functional groups could partially close or block the pore openings even after conversion into N-functional groups by reacting with cyanamide.[6a,16] By contrast, a treatment with cyanimide in absence of a pre-oxidation step etches the pore openings and broadens their size, as also reported effect in literature.[17] In both cases, the pore openings are the most vulnerable sites, because an edge in the carbon matrix causes unsaturated sites, making them the weakest point. After ionomer coating and electrode manufacturing, the altered pore structure of the support did not change the gravimetric stacking volume of the catalytic layer significantly (Table S2). Since the layer porosity throughout the electrode is directly proportional to the gravimetric stacking volume, it did not change, either. As a result of this, any changes in the MEA performance cannot be attributed to mass transport issues on a macroscopic level of the catalytic layer, but rather must arise from processes at the micro/nano scale.

N-modification cannot only change the pore structure of a carbon support but can influence the interaction with the ionomer during the catalyst layer manufacturing process, as well. In our recent publications, we demonstrated that N-groups in the carbon lattice are able to strongly interact with the negatively charged side chains of the ionomer resulting in more evenly distributed ionomer layer over the catalyst surface.[6b] Hence, in the present study to gain a better understanding of the ionomer distribution and the accessibility of the active sites as a result of the structural changes of the carbon support, we conducted CO stripping measurements at different relative humidities.

Correlation of Pt-accessibility and ionomer coverage

The determination of the ECSA via CO stripping at different relative humidities gives information about the Pt surface accessibility.[18] After CO adsorption on the Pt sites, an anodic scan can electrochemically oxidize CO to CO_2 only in the presence of oxygenated surface groups such as -OH. Under dry operating conditions (< 40 % RH), -OH groups are available for electrochemical stripping of CO from Pt, if and only if those sites are located in close proximity to the ionomer. By contrast, under wet conditions (high relative humidities > 70 % RH) water is omnipresent within the catalytic layer and all the Pt sites are electrochemical accessible for CO stripping. The ratio of two experimental ECSA values at different humidity yields the so-called "Pt-accessibility" in the catalyst layer. Figure 2 shows all four Pt-accessibilities normalized with respect to the absolute ECSA value of Pt/CMK-3. It is evident that the catalysts supported on CMK-3 and CMK-3/CA showed enhanced electrochemical utilization over the other two. While the Pt accessibility describes the interface between ionomer and Pt surface, it fails to provide insight into the ionomer coverage over the entire catalyst (i.e. the ionomer interface of the ionomer with carbon/Pt). For this reason, we evaluated the double layer

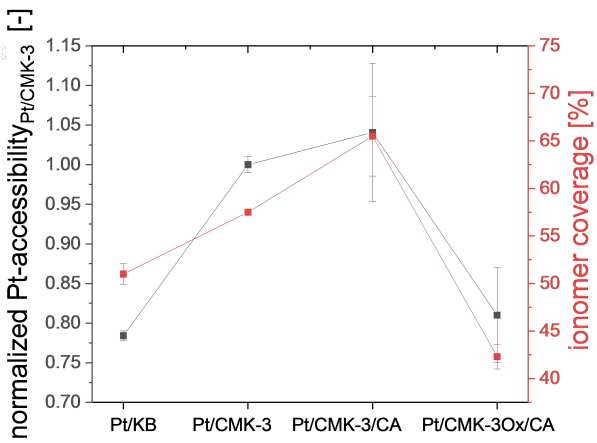

Figure 2. An overview of the normalized Pt-accessibility factor and the ionomer coverage descriptor with respect to the different types of catalyst prepared with different types of carbon support. Pt-accessibility factor (left axis in black) gives the ratio of the $ECSA_{30RH}/ECSA_{100RH}$ normalized to Pt/CMK-3 Pt accessibility, whereas the ionomer coverage factor describes CDL_{30RH}/CDL_{100RH} (right axis in red).

© 2021 The Authors. ChemCatChem published by Wiley-VCH GmbH

capacitance at different relative humidities. In the regime of 0.45 V under the operation conditions of H_2/N_2 (anode/cathode), neither of the ORR, OER, HOR or HER current is contributing to the cyclic voltammogram. Hence, the electron transfer originates exclusively from double layer and pseudo-capacitive currents. This double layer is built up at the interface between carbon/Pt and water/ionomer. Under dry conditions, it is reasonable to assume all water to be trapped in the hydrophilic ionomer, implying that the double layer interfaces only build up between ionomer and carbon or Pt. Thus, the double layer capacity could be directly correlated with the ionomer distribution. On the other hand, under wet conditions, liquid water will be present over the entire catalyst surface due to water condensation and capillary forces in pores, which will then render most of the Pt electrochemically active. The ratio of the double layer from dry to wet conditions than can be used as an "ionomer coverage" descriptor, also plotted in Figure 2.

Figure 2 reveals a very similar trend and correlation between the ionomer coverage and Pt accessibility. As expected, Pt-accessibility is directly linked with ionomer coverage, as it is a direct measure of the ionomer distribution and the electrochemical accessibility under dry conditions. After N-modification, a moderate increase and a drastic decrease in ionomer coverage was discernible for Pt/CMK-3/CA and Pt/CMK-3Ox/CA, respectively. Based on the latter, we can conclude that we are looking at a set of catalysts with a homogenous ionomer distribution (i.e. Pt/CMK-3 and Pt/CMK-3/CA) and another one with a rather inhomogeneous one (Pt/KB and Pt/CMK-3Ox/CA). Interestingly, the Pt-accessibility factor does not go down to the same extent as the ionomer coverage. It appears that Pt/KB displays a lower than expected accessibility factor compared to Pt/CMK-3, if one would expect the ionomer coverage to be the only parameter defining Pt-accessibility. Hence, we can say that the ionomer coverage influences both the ECSA under dry conditions and the Pt-accessibility. However, as we will show now, another parameter must be considered to account for this discrepancy; reveals that Pt-accessibility is not linearly correlating with the ionomer coverage.

Correlation of dry ECSA with the pore structure in the CL

Figure 3 reveals a surprising, yet clear correlation between the ECSA at 30% RH and the pore opening diameter. This indicates that the electrochemically active Pt sites are only those that in close contact with the ionomer, which serves as the only surface oxygenate-supplying phase under these dry conditions. A possible explanation for this correlation lies in the effect that broader pore openings can enable a better penetration of the ionomer into the pore structure reaching out for the Pt sites. This is in agreement with the findings of Yarlaggada et al. describing a enhanced Pt-utilization and better penetration of the ionomer into the pores for carbon revealing a higher fraction of pores in the range of 4–7 nm.[4b] In contrast to this, smaller pores would tend to be either blocked by larger Pt particles or the ionomer chain would not be able to penetrate

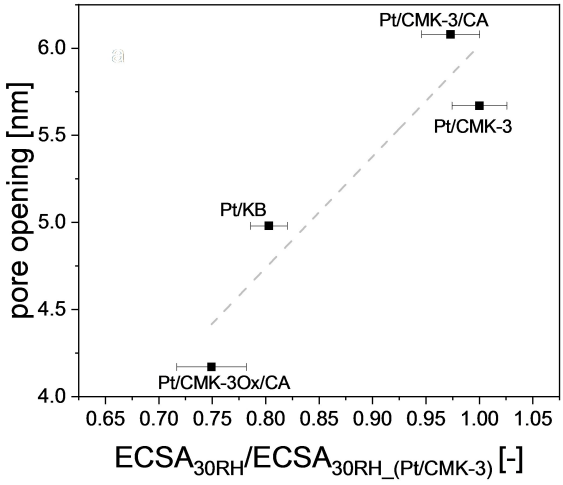

Figure 3. Correlation of supports' pore opening with relative ECSA values of their MEAs, comprising cathodic CLs with various carbon supports, at. 30% RH. The ECSA values for all the catalysts were normalized to the ECSA value of Pt/CMK-3, as it exhibited the highest performance and highest ECSA. The pore openings were extracted from N_2 physisorption pores area distribution plot as given in Figure 1.

the pore, thus making the Pt particles located inside the pore inaccessible. Additionally, the increased Pt-particle size of Pt/CMK-3Ox/CA reduced the overall ECSA compared to the other catalysts. The relation of the catalyst layer ECSA with oxygen mass transport resistance and the resulting performance has been repeatedly emphasized in recent work.[19] A higher number of catalytic active sites per mass of catalyst or per geometric area of catalyst layer limits the local oxygen flux to the Pt surface under dominating mass transport conditions present at high current densities.

Correlation of MEA performance and ECSA values

The ECSA value under dry (e.g. 30% RH) operating conditions depends on the ionomer coverage and Pt accessibility, where it controls the high current cell performance, as demonstrated in Figure 4a. The dry ECSA values are a measure of the number of accessibility active Pt surface sites and evidently correlate with the carbon porous structure. The choice of 1.0 A/cm^2 in Figure 4a aids to facilitate direct correlation with other graphs in this contribution. However, the impact of the dry ECSA value becomes more and more pronounced at higher current densities. As an example, the cell voltage of Pt/CMK-3Ox/CA drops below that of Pt/KB at 1.2 A/cm^2 (cf Figure 8). By contrast, under wet operation conditions (Figure 4b), there is no significant correlation between cell performance and (wet) ECSA. This is because liquid water compensates as proton conducting medium for site disconnecting from the ionomer. Consequently, all Pt sites will be electrochemically accessible and the MEA performance no longer scales with ECSA / Pt-accessibility. However, water accumulation and local flooding effects form the origin of the observed mass transport losses for the case of Pt/CMK-3 Ox/CA, due to inhomogeneous ionomer

© 2021 The Authors. ChemCatChem published by Wiley-VCH GmbH

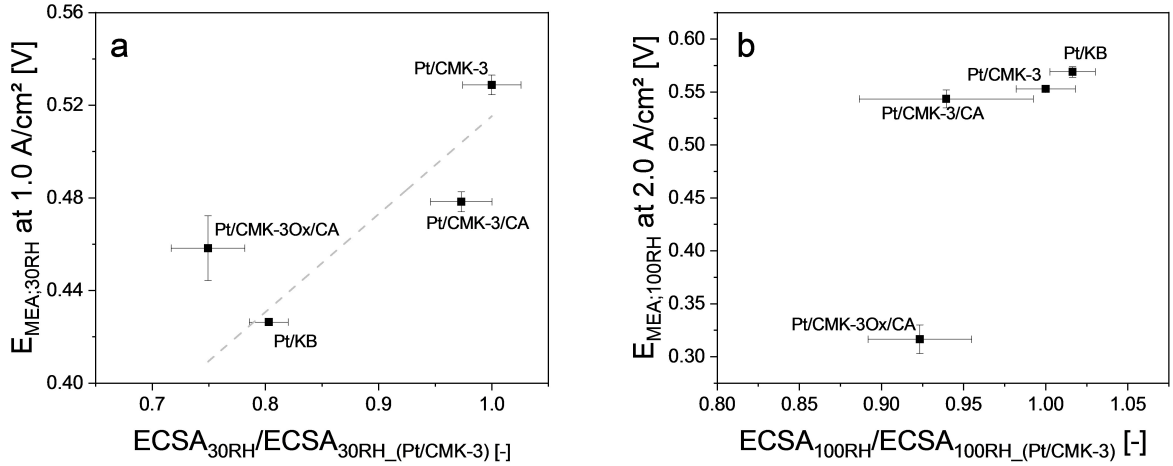

Figure 4. Correlation of performance of 5 cm² MEAs, comprising cathodic CLs with various carbon supports, with their relative ECSA values at each respective relative humidity: a. 30% RH and b. 100% RH. For each RH, the ECSA values for all the catalysts were normalized to the ECSA value of Pt/CMK-3, as the latter exhibited the highest performance and ECSA values. Cell voltage determined at (a) 1.0 A/cm² at 90 °C and 30% RH, while (b) at 2.0 A/cm² at 60 °C, 90% RH. Backpressure of 170 kPa_{abs} were applied for both anode and cathode compartments. Error bars represent the mean absolute deviation from two independent measurements.

distribution (see Figure 2) combined with an unfavorable pore structure of the catalyst layer.

Catalyst layer (CL) porosity

To characterize the impact of material components on the catalyst layer properties, and to account for the observations and conclusions of Figure 4, the pore size distribution of the cathode catalyst/ionomer layer was investigated by means of N_2 adsorption where a QSDFT kernel using cylindrical pore models was used for analysis. Figure 5 displays the resulting differential porous surface area distribution, dS(d) [m²/nm/g] against the pore size (width). Here, the surface area that is directly represented by the area under the curve.[10a] Figure 5 reveals the origin of the poor wet MEA performance of the "CMK-3Ox/CA" support in Figure 4: The high fraction of micropores < 2 nm (red curve in Figure 5) in the CL benefits water accumulation due to capillary forces. The accumulated water is speculated, to cause local flooding resulting in increased mass transport resistance. The flooding of the Pt/CMK-3Ox/CA CL is further compounded by an unfavorable ionomer coverage (Figure 2). The reference CL, Pt/KB, showed a similar ratio between micro- and mesopores across the layer. By contrast, the well performing CLs, Pt/CMK-3/CA and Pt/CMK-3, were found to have a more homogenous ionomer distribution. The latter was based on a more prevalent mesopore ratio near the 5 nm pore size width, in combination to the minor contributions from micropores (< 2 nm pore width).

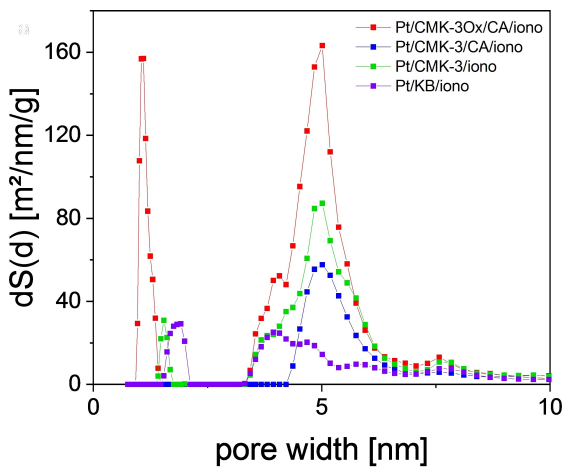

Figure 5. Pore area distributions of the catalyst material with different types of carbon supports (unmodified and N-functionalized) calculated by the QSDFT model and based on the adsorption branch. The graph shows the derivative of the pore surface with respect to the pore diameter vs. the pore diameter for the different catalyst layers (catalyst + ionomer).

Oxygen transport resistance

The ECSA values of our four CLs control the observed mass transport effects and layer resistances.[19] As demonstrated above, the ECSA values are a strong function of the support pore structure and the individual ionomer distribution. Limiting current measurements yield quantitative insight in oxygen transport resistances within the CL that affect the MEA performance. Data from limiting current measurements allow for deconvolution of oxygen transport losses originating from the CL and GDL, into pressure-dependent (PD) and pressure-independent (PI) contributions. R_{PI} resistances (originating mainly in the CL) can be further split into i) a so-called "local" oxygen diffusion resistance at the ionomer-covered Pt interface, and ii) into a Knudsen pore diffusion resistance. Harada et al. provided the first structural evidence of the local transport resistance. They showed that ionomer films on top of a

© 2021 The Authors. ChemCatChem published by Wiley-VCH GmbH

platinum nanoparticles revealed higher density causing additional transport resistance for molecular oxygen.[20] The Knudsen resistance, on the other hand, describes the oxygen transport through a porous material when a single molecule is rather restricted in movement by the pore walls instead of interaction with other molecules. This factor will be influenced by the ionomer coverages that determines the effective pore structure within the catalytic layer.[6b]

We conducted limiting current measurements at 30% and 100% RH to mimic dry and wet operating conditions, respectively. In doing so, we followed Baker et al.'s approach to estimate the PI oxygen mass transport resistance, R_{PI}, from limiting current measurements by varying the partial pressure of oxygen in the cathode feed.[13,21] Figure 6a shows that the MEA performance under dry conditions at 1.0 A/cm^2 correlates very well with estimates of R_{PI}. Interestingly, even though the KB-based CL had the thinnest ionomer film layer (Table 3), its R_{PI} is comparably high (Figure 6a). This can be attributed to the reduced pore opening diameter of KB, offsetting the beneficial effect of the thin ionomer layer. Surprisingly, the Pt/CMK-3Ox/CA CL displayed a similar R_{PI} as the Pt/CMK/CA despite its unfavorable pore opening and ionomer distribution characteristics (cf Figures 2, 3). This can be rationalized based on the influence of the proton transport under dry operating conditions on the effective pressure independent resistance term, R_{PI}.[22] Hence, the relatively low R_{PI} value of Pt/CMK-3Ox/CA is also attributed to its favorably low proton transport resistance under low RH, which will be discussed further below. Finally, the CLs Pt/CMK-3 and Pt/CMK-3/CA featuring broader and better accessible pores in combination with favorable ionomer distribution and high ECSA values show the lowest R_{PI} values.

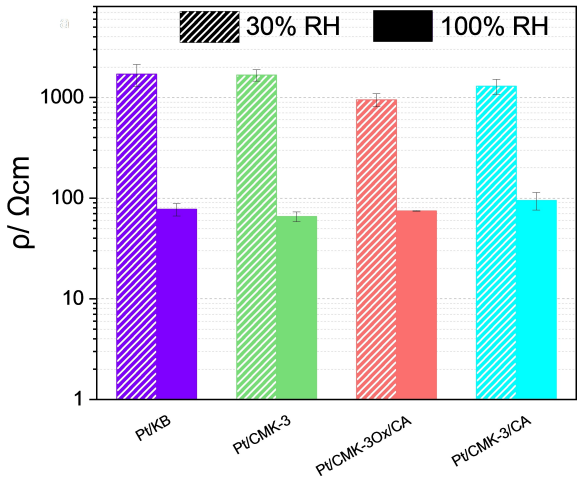

Figure 7. Effect of relative humidity on the proton resistivity of the cathode CL comprising different types of catalyst. The proton resistivity was determined from impedance spectroscopy in H_2/N_2 via fitting with a transmission line model. Conditions for the impedance are: cell temperature of 80 °C, as well as 100% RH (solid bar) or 30% RH (dashed bar). Error bars represent the mean absolute deviation from two independent measurements.

Proton conductivity in cathode CL

Good cell performance requires sufficient supply of protons, especially under dry operating conditions. Proton-conduction rates across the catalyst layer are controlled by the specific proton resistivity, ρ, extracted from impedance data using the transmission line equivalent circuit model (Figure S5). Catalytic layers with varying ionomer distributions and tortuosities can provide comparable proton resistivity values on a macroscopic level.[10a] Figure 7 reports the proton transport resistivities of our four CLs determined from EIS, where the experimental data

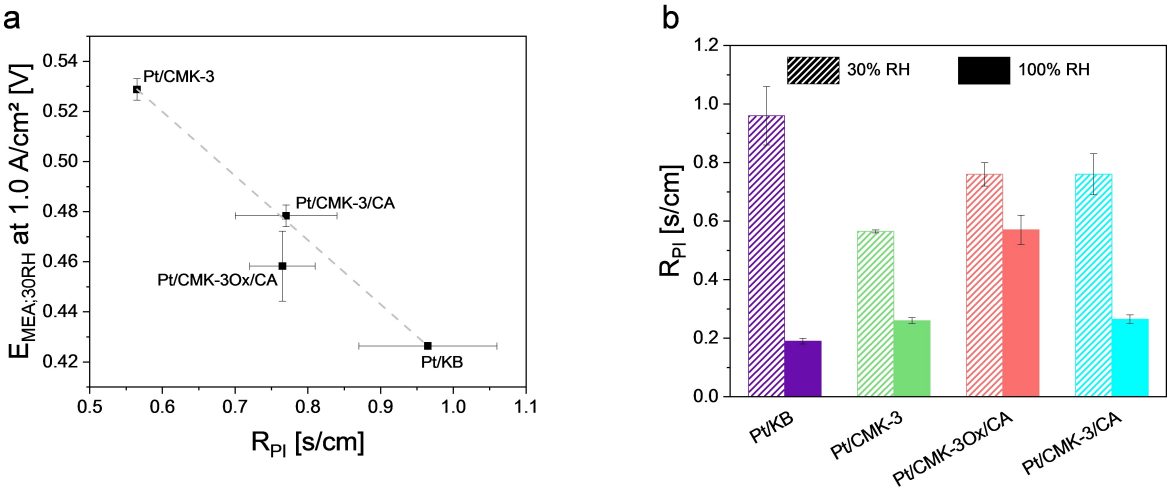

Figure 6. (a) Correlation of performance of 5 cm^2 MEAs, comprising cathodic CLs with various carbon supports, with their pressure independent O_2 mass transport term R_{PI} at. 30% RH. Cell voltage determined at 1.0 A/cm^2 at 90 °C and 30% RH with a backpressure of 170 kPa$_{abs}$ were applied for both anode and cathode compartments (b) Comparison of O_2 mass transport resistance pressure independent term (R_{PI}). The measurements were conducted at 80 °C and at 100% RH (solid bar) or 30% RH (dashed bar). Absolute pressures were set at 170 kPa$_{abs}$ on both anode and cathode sides. The error bars correspond to the standard deviation between independent measurements with two different MEAs for each type of catalyst layer.

© 2021 The Authors. ChemCatChem published by Wiley-VCH GmbH

were fitted with a transmission line model equivalent circuit as illustrated in Figure S6 and S7. The CL comprising Pt/CMK-3Ox/CA revealed the lowest proton resistivity, even though the ionomer of this CL is less homogenously distributed compared to Pt/CMK-3 and Pt/CMK-3/CA. A possible explanation lies in the "effective" ionomer film thickness. A certain amount of the ionomer will intrude into internal pore voids of the primary carbon particle and therefore will not take part in the ionomer film covering the external catalyst surface. Liu et al. found a correlation between the intruded ionomer fraction and the pore volume of pores <4 nm. We note that an intrusion of the ionomer into small micropores of <1 nm is physically unlikely.[11] Thus, the larger the ionomer ratio that intrudes, the thinner the remaining effective ionomer film that covers the catalyst. As a consequence, the proton resistivity (in Ω·cm) of the effective ionomer film increases. Among the four CLs under investigation under dry operating conditions the CL Pt/CMK-3/Ox revealed the lowest proton transport resistivity at an effective film thickness of around 1.27 nm. Increased resistivities were obtained for Pt/KB and Pt/CMK-3 CLs with an effective ionomer film of thickness <0.5 nm (see Table 3).

Under wet operating conditions, liquid water will compensate the reduced effective ionomer film thickness. Now, proton resistivity is no longer determined by the film thickness alone. As a result of this, under dry operating conditions, the pressure independent mass transport resistance, R_{PI}, is affected by the additional proton transport resistance and molecular oxygen mass transport resistance, as shown in Figure 6.

As expected the proton resistivity is lower under 100% RH compared to 30% RH. The experimental ρ-values obtained from the of the Pt/KB based CL utilizing low EW type ionomer, and its I/C ratio, is in excellent agreement with literature data under comparable conditions.[4a] We note that the accuracy of the transmission line model under high humidity suffers from a relatively large error. Taking this in consideration, the observed differences in proton resistivity among the four CLs can be considered insignificant. In addition, these values cannot account for the observed changes in performance under wet operating conditions (cf Figure 4). Therefore, under such high relative humidity operating conditions, structural or other physico-chemical properties of the CL may explain the ab- or presence of electrode flooding.

Effect of pore structure on PEMFC performance

Figure 8 shows the corresponding polarization curves of MEAs comprising the differently modified catalytic layers. The polarization curves were obtained using 5 cm^2 MEAs under two extreme operating conditions, at 60 °C and 90% RH, herein defined as "wet operating conditions"; and at 90 °C and 30% RH, herein defined as "dry operating conditions. All tested MEAs had an average cathode catalyst loading of 0.129±

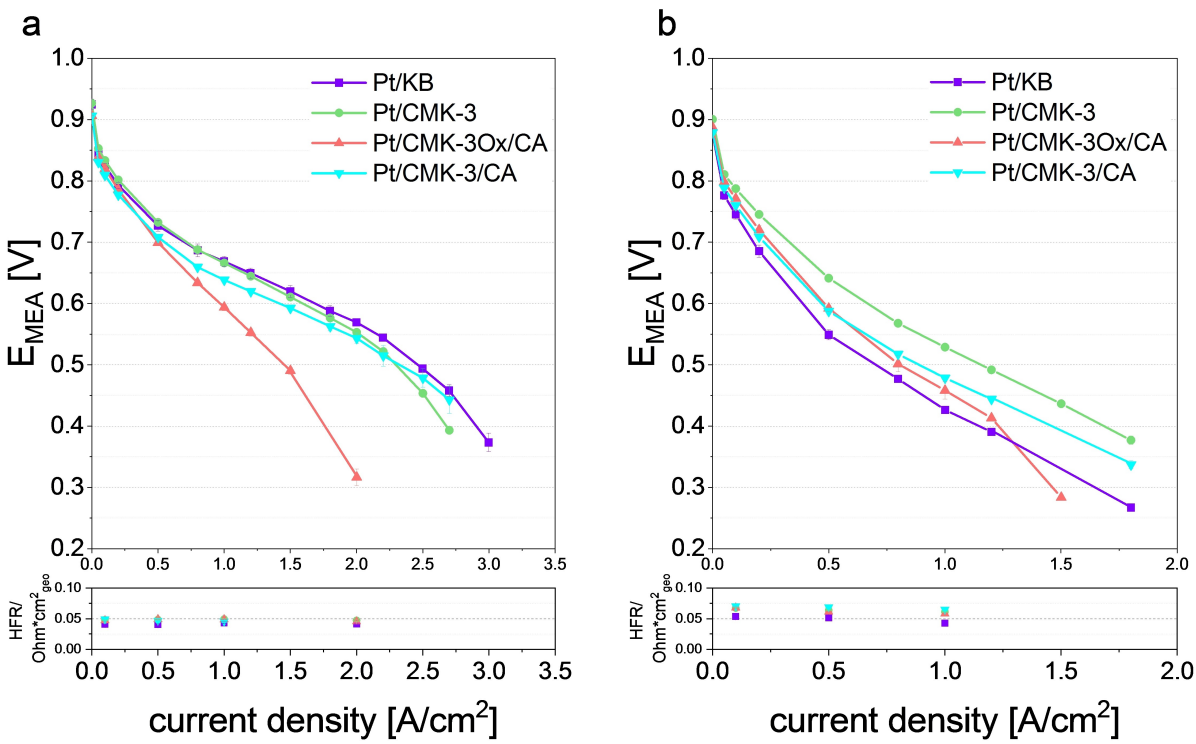

Figure 8. MEA performance, comprising of different cathodic catalyst layers, under cell temperature of 60 °C with 90% RH (a) and under cell temperature of 90 °C with 30% RH (b) with a backpressure of 170 $kPa_{abs,out}$ for both anode and cathode compartments. Polarization curves were measured under constant differential flow (H_2: 1.0 Nl/min and air: 2.0 Nl/min). The voltage was corrected for the monopolar plate resistance (0.0345 Ω cm^2). Error bars represent the mean absolute deviation from two independent measurements.

© 2021 The Authors. ChemCatChem published by Wiley-VCH GmbH

0.013 mg_{Pt}/cm^2 and an ionomer to carbon mass ratio (I/C) of 0.65. As also discussed in earlier parts of the manuscript (Figure 4), a clear flooding tendency of Pt/CMK-3Ox/CA catalyst layer gets discernible under wet operating conditions (Figure 7a), which can be mainly attributed to the bad ionomer coverage leading to blockage of certain pores within the catalytic layer. Despite the Pt/KB electrode having a slightly lower Pt loading compared to the other catalyst layers, it exhibits the highest performance under wet operating conditions. Hence, any observed difference in performance cannot be rationalized by an alteration in Pt loading of the MEA or by changes in ESCA (which is already normalized to the Pt loading). On the other hand, the presence of high fractions of micropore volume after ionomer coating(Figure 5) benefits water accumulation, as a result of capillary forces, which would then result in an increase mass transport resistance at high current densities. The ionomer and pore size distribution throughout the catalytic layer of the other three catalysts prevent a significant cell flooding thus their performance does not alter significantly from each other.

Under dry operating conditions, the performance of the MEA strongly depends on the ionomer distribution and ECSA since there is no excess of water to compensate for any discontinuity in the ionomer film over the catalysts' surface. Figure 7b clearly shows the improved performance of CLs based on CMK-3 or CMK-3/CA when used as supporting material. The beneficial pore structure and pronounced porosity in the range of 3–6 nm enables a good Pt accessibility and combined with a tailored N-modification a homogenous ionomer distribution, as opposed to a conventional KB carbon support. This in turn points out the importance of the structural and physicochemical property of the support material itself. A well-defined pore structure revealing pore openings in the range of 3–6 nm improve the Pt accessibility due to enhanced ionomer penetration without blocking essential pore structure for oxygen mass transport. The increased ECSA alongside with reduced mass transport resistance, optimizes the transport phenomena within the catalytic layer. Pt/CMK-3 combines those benefits together with a sufficient protonic conductive pathway on a macroscopically scale. Generally speaking, the performance goes up with the pore openings (Figure 3) of the supporting material. This clearly shows the importance of the supports' mesoporous structure for both the activity of the catalyst and also its performance as well.

Conclusion

This experimental study highlights the important role of controlled mesoporosity of a high performing PEMFC cathode catalyst support material. A well-defined CMK-3 support was chemically treated and its pore structure tuned. A detailed investigation of such structural modified support materials was conducted under two extreme MEA operating conditions: wet (at 60 °C, 90 % RH) and dry (at 90 °C, 30 % RH). The combination of these two working conditions as well as a detailed analysis of the support material and the catalytic layer via N_2-physisorption enables us to explain the improved performance of Pt/CMK-3.

A well-defined pore structure in the range of 3–6 nm enables a deeper penetration of the ionomer into and over the surface of the Pt particles. Following this, all active sites tend to be in close proximity of the ionomer, consequently increasing ECSA values even under dry operating conditions. Additionally, mesoporous support material combined with homogenous ionomer distribution construct a catalytic layer with favored pore size distribution for oxygen and water transport. Thus, preventing water accumulation and at the same time reducing oxygen mass transport resistance towards the active sites.

In the present study, we have demonstrated the importance of a well-defined mesoporous support structure. Recommendations for preferable porosity characteristics are provided in the range of 3–6 nm in absence of microporosity for not only the increase in catalyst activity, but also towards its overall performance. Future studies in developing new catalyst materials for fuel cell applications shall consider the role the support material in the same extent as the active material itself, including their interplay, which could crucially influence catalyst layer performance.

Acknowledgement

This work was supported by the BMW Group. The authors would also like to thank the members of FC Test Field, FC Technology Development and Technology Material Analysis of BMW Group for their support during Fuel cell testing, MEA manufacturing and decal preparation. Open Access funding enabled and organized by Projekt DEAL.

Conflict of Interest

The authors declare no conflict of interest.

Keywords: oxygen reduction reaction · fuel cell · mass transport · porosity · catalyst layer

[1] (https://energy.gov/sites/prod/files/2014/02/f8/fctt_roadmap_june2013.pdf) **08/21/18**.
[2] L. Pan, S. Ott, F. Dionigi, P. Strasser, *Curr. Opin. Electrochem.* **2019**, *18*, 61–71.
[3] Y.-C. Park, H. Tokiwa, K. Kakinuma, M. Watanabe, M. Uchida, *J. Power Sources* **2016**, *315*, 179–191.
[4] a) G. S. Harzer, A. Orfanidi, H. El-Sayed, P. Madkikar, H. A. Gasteiger, *J. Electrochem. Soc.* **2018**, *165*, F770–F779; b) V. Yarlagadda, M. K. Carpenter, T. E. Moylan, R. S. Kukreja, R. Koestner, W. Gu, L. Thompson, A. Kongkanand, *ACS Energy Lett.* **2018**, *3*, 618–621.
[5] A. Z. Weber, A. Kusoglu, *J. Mater. Chem. A* **2014**, *2*, 17207–17211.
[6] a) A. Orfanidi, P. Madkikar, H. A. El-Sayed, G. S. Harzer, T. Kratky, H. A. Gasteiger, *J. Electrochem. Soc.* **2017**, *164*, F418–F426; b) S. Ott, A. Orfanidi, H. Schmies, B. Anke, H. N. Nong, J. Hubner, U. Gernert, M. Gliech, M. Lerch, P. Strasser, *Nat. Mater.* **2020**, *19*, 77–85.
[7] K. Kodama, K. Motobayashi, A. Shinohara, N. Hasegawa, K. Kudo, R. Jinnouchi, M. Osawa, Y. Morimoto, *ACS Catal.* **2017**, *8*, 694–700.
[8] V. C. Yarlagadda, K. Michael, T. E. Moylan, R. S. Kukreja, R. Koestner, W. Gu, L. Thompson, A. Kongkanand, *ACS Energy Lett.* **2018**, *3*, 618–621.

© 2021 The Authors. ChemCatChem published by Wiley-VCH GmbH

[9] N. Ramaswamy, W. Gu, J. M. Ziegelbauer, S. Kumaraguru, *ECS* **2020**, *167*, 064515.
[10] a) A. Orfanidi, P. J. Rheinlander, N. Schulte, H. A. Gasteiger, *J. Electrochem. Soc.* **2018**, *165*, F1254–F1263; b) G. Y. Gor, M. Thommes, K. A. Cychosz, A. V. Neimark, *Carbon* **2012**, *50*, 1583–1590; c) A. V. Neimark, Y. Lin, P. I. Ravikovitch, M. Thommes, *Carbon* **2009**, *47*, 1617–1628.
[11] Y. Liu, C. Ji, W. Gu, J. Jorne, H. A. Gasteiger, *ECS* **2011**, *158*, B614–B621.
[12] K. Shinozaki, Y. Morimoto, B. S. Pivovar, S. S. Kocha, *J. Power Sources* **2016**, *325*, 745–751.
[13] D. R. Baker, C. A. Caulk, K. C. Neyerlin, M. W. Murph, *J. Electrochem. Soc.* **2009**, *156*, B991–B1003.
[14] F. Du, T. A. Dao, P. V. J. Peitl, A. Bauer, K. Preuss, A. M. Bonastre, J. Sharman, G. Spikes, M. Perchthaler, T. J. Schmidt, A. Orfanidi, *J. Electrochem. Soc.* **2020**, *167*, 144513.
[15] T. K. Sherwood, E. R. Gilliland, S. W. Ing, *Ind. Eng. Chem.* **1960**, *52*, 601–604.
[16] M. Toupin, D. Be'langer, *Langmuir* **2008**, *24*, 1910–1917.
[17] F. Jaouen, J.-P. Dodelet, *J. Phys. Chem. C* **2007**, *111*, 5963–5970.
[18] a) E. Padgett, N. Andrejevic, Z. Liu, A. Kongkanand, W. Gu, K. Moriyama, Y. Jiang, S. Kumaraguru, T. E. Moylan, R. Kukreja, M. D. A., *ECS* **2018**, *165*, F173–F180; b) E. Padgett, V. Yarlagadda, M. E. Holtz, K. Ko, B. D. A. Levin, R. S. Kukreja, J. M. Ziegelbauer, R. N. Andrews, J. Ilavsky, A. Kongkanand, D. A. Muller, *ECS* **2019**, *166*, F198–F207.
[19] A. Kongkanand, M. F. Mathias, *J. Phys. Chem. Lett.* **2016**, *7*, 1127–1137.
[20] M. Harada, K. Kudo, N. L. Yamada, *Chem. Lett.* **2019**, *48*, 51–54.
[21] D. A. Caulk, D. R. Baker, *J. Electrochem. Soc.* **2010**, *157*, B1237–B1244.
[22] N. Nonoyama, S. Okazaki, A. Z. Weber, Y. Ikogi, T. Yoshida, *ECS* **2011**, *158*, B416–B423.

Manuscript received: August 3, 2021
Revised manuscript received: September 8, 2021
Accepted manuscript online: September 14, 2021
Version of record online: September 27, 2021

© 2021 The Authors. ChemCatChem published by Wiley-VCH GmbH